Universal Hydrodynamic Mechanisms for Crystallization in Active Colloidal Suspensions

Rajesh Singh* and R. Adhikari†
The Institute of Mathematical Sciences-HBNI, CIT Campus, Chennai 600113, India
(Received 17 June 2016; published 23 November 2016)

The lack of detailed balance in active colloidal suspensions allows dissipation to determine stationary states. Here we show that slow viscous flow produced by polar or apolar active colloids near plane walls mediates attractive hydrodynamic forces that drive crystallization. Hydrodynamically mediated torques tend to destabilize the crystal but stability can be regained through critical amounts of bottom heaviness or chiral activity. Numerical simulations show that crystallization is not nucleational, as in equilibrium, but is preceded by a spinodal-like instability. Harmonic excitations of the active crystal relax diffusively but the normal modes are distinct from an equilibrium colloidal crystal. The hydrodynamic mechanisms presented here are universal and rationalize recent experiments on the crystallization of active colloids.

DOI: 10.1103/PhysRevLett.117.228002

In active colloidal suspensions [1,2] energy is continuously dissipated into the ambient viscous fluid. The balance between dissipation and fluctuation that prevails in equilibrium colloidal suspensions [3,4] is, therefore, absent. Nonequilibrium stationary states in active suspensions, then, are determined by both dissipative and conservative forces, quite unlike passive suspensions where detailed balance prevents dissipative forces from determining phases of thermodynamic equilibrium. In this context, it is of great interest to enquire how thermodynamic phase transitions driven by changes in free energy are modified in the presence of sustained dissipation.

In two recent experiments, disordered suspensions of active colloids have been observed to spontaneously order into two-dimensional hexagonal crystals when confined at a plane wall. Bottom-heavy synthetic active colloids which catalyze hydrogen peroxide when optically illuminated are used in the first experiment [1], while chiral fast-swimming bacteria of the species *Thiovulum majus* are used in the second experiment [2]. Given this remarkably similar crystallization in two disparate active suspensions, it is natural to ask if the phenomenon is universal and to search for mechanisms, necessarily involving dissipation, that drive it.

Our current understanding of phase separation in particulate active systems is derived from the coarse-grained theory of motility-induced phase separation (MIPS), where active particles are advected by a density-dependent velocity [5]. Microscopic models with kinematics consistent with MIPS also show phase separation and crystallization of hard active disks have been reported in two dimensions [6]. However, these models ignore exchange of the locally conserved momentum of the ambient fluid with that of the active particles and are, thus, best applied to systems where such exchanges can be ignored. Fluid flow is an integral part of the physics in Refs. [1,2] and a momentum-conserving theory, currently lacking, is essential to identify the dissipative forces and torques that drive crystallization.

In this Letter, we present a microscopic theory of active crystallization that connects directly to the experiments described above. Specifically, we account for the *three-dimensional* active flow in the fluid and the effect of a plane wall on this flow. Representing activity by slip in a thin boundary layer at the colloid surface [7] we rigorously compute the long-ranged many-body hydrodynamic forces and torques on the colloids. Thus, we estimate Brownian forces and torques to be smaller than their active counterparts by factors of order 10^2 (for synthetic colloids in Ref. [1]) to 10^4 (for bacteria in Ref. [2]) making them largely irrelevant for active crystallization. We integrate the resulting deterministic balance equations numerically to obtain dynamical trajectories.

Our main numerical results are summarized in Fig. (1). Panels (a)–(c) show the spontaneous destabilization of the uniform state by attractive active hydrodynamic forces, the formation of multiple crystallites, and their coalescence into a single hexagonal crystal at late times. Panels (d)–(f) show the structure factor at corresponding times. The route to crystallization is not through activated processes that produce critical nuclei, but through a spinodal-like instability produced by the unbalanced long-ranged active attraction. The uniform state is, therefore, always unstable and crystallization occurs for all values of density, in contrast to the finite density necessary for crystallization in MIPS models [5]. Active hydrodynamic torques tend to destabilize the ordered state but stability is regained when these are balanced by external torques (from bottom-heaviness in Ref. [1]) or by chiral activity (from bacterial spin in Ref. [2]). Crystallites of chiral colloids rotate at an angular velocity that is inversely proportional to the number of colloids contained in them, as shown in panel (g). This is in excellent agreement with the experiment of Ref. [2]. The critical values of bottom heaviness and chirality above which orientational stability, and, hence, positional order, is ensured is shown in panel (h). We now present our model and detail the derivation of our results.

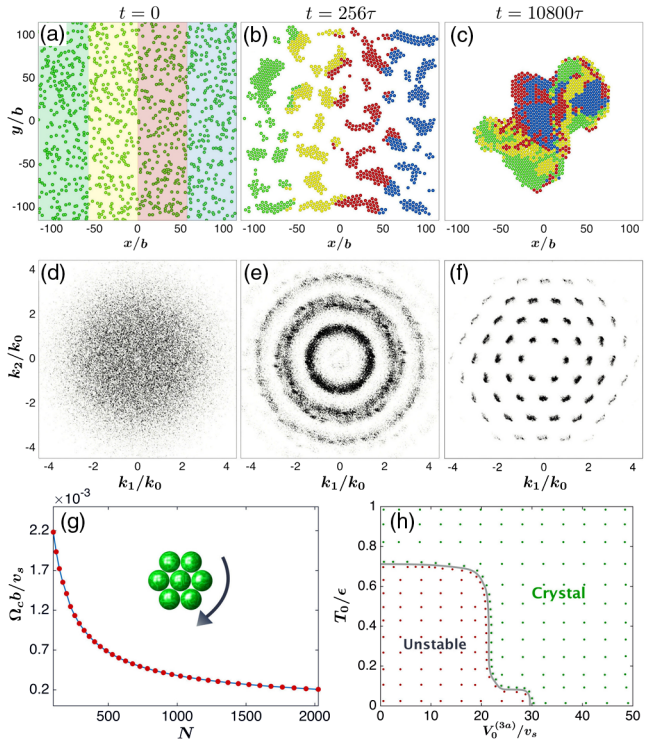

FIG. 1. Panels (a)–(c) are instantaneous configurations during the crystallization of 1024 active colloids of radius b at a plane wall. The colloids are colored by their initial positions. Panels (d)–(f) show the structure factor $S(\mathbf{k})$ at corresponding instants. Wave numbers are scaled by the modulus of the reciprocal lattice vector k_0 and the contribution from $\mathbf{k}=0$ is discarded. Panel (g) shows the variation of the angular velocity Ω_c of a crystallite with the number N of colloids in it. A typical configuration is shown in the inset. Panel (h) is the state diagram for orientational stability in terms of the measure of chirality $V_0^{(3a)}$ and bottom heaviness T_0 (see text). Each dot represents one simulation. Here, v_s is the self-propulsion speed of an isolated colloid, $\tau = b/v_s$, and ϵ is the scale of the repulsive steric potential.

Model.—We consider N spherical active colloids of radius b near a plane wall with center-of-mass coordinates $\mathbf{R}_i$, orientation $\mathbf{p}_i$, linear velocity $\mathbf{V}_i$, and angular velocity Ω_i, where $i = 1 \ldots N$. Activity is imposed through a slip velocity $\mathbf{v}_i^{\mathcal{A}}$, which is a general vector field on the surface S_i of the ith colloid satisfying $\int \hat{\boldsymbol{\rho}}_i \cdot \mathbf{v}_i^{\mathcal{A}} d\mathrm{S}_i = 0$ [8], where $\boldsymbol{\rho}_i$ is the vector from center of the colloid to a point on its surface. The fluid velocity $\mathbf{v}$ is subject to slip boundary conditions

$$\mathbf{v}(\mathbf{R}_i + \boldsymbol{\rho}_i) = \mathbf{V}_i + \Omega_i \times \boldsymbol{\rho}_i + \mathbf{v}_i^{\mathcal{A}}(\boldsymbol{\rho}_i) \tag{1}$$

on the colloid surfaces, to a no-slip boundary condition $\mathbf{v} = 0$ at the plane wall located at $z = 0$, and to a quiescent boundary condition at large distances from the wall. The slip is conveniently parametrized by an expansion $\mathbf{v}^{\mathcal{A}}(\mathbf{R}_i + \boldsymbol{\rho}_i) = \sum_{l=1}^{\infty} [1/(l-1)!(2l-3)!!] \mathbf{V}_i^{(l)} \cdot \mathbf{Y}^{(l-1)}(\hat{\boldsymbol{\rho}}_i)$ in irreducible tensorial spherical harmonics $\mathbf{Y}^{(l)}(\hat{\boldsymbol{\rho}}) = (-1)^l \rho^{l+1} \boldsymbol{\nabla}^{(l)} \rho^{-1}$, where $\boldsymbol{\nabla}^{(l)} = \boldsymbol{\nabla}_{\alpha_1} \ldots \boldsymbol{\nabla}_{\alpha_l}$. The expansion coefficients $\mathbf{V}_i^{(l)}$ are lth rank reducible Cartesian tensors with three irreducible parts of ranks l, $l-1$, and $l-2$, corresponding to symmetric traceless, antisymmetric, and pure trace combinations of the reducible indices. We denote these by $\mathbf{V}_i^{(ls)}$, $\mathbf{V}_i^{(la)}$, and $\mathbf{V}_i^{(lt)}$, respectively. The leading contributions from the slip,

$$\mathbf{v}_i^{\mathcal{A}}(\boldsymbol{\rho}_i) = \underbrace{-\mathbf{V}_i^{\mathcal{A}} + \frac{1}{15}\mathbf{V}_i^{(3t)} \cdot \mathbf{Y}^{(2)}}_{\text{achiral,polar}} \underbrace{- \frac{1}{9}\boldsymbol{\epsilon} \cdot \mathbf{V}_i^{(3a)} \cdot \mathbf{Y}^{(2)}}_{\text{chiral,apolar}} + \underbrace{\mathbf{V}_i^{(2s)} \cdot \mathbf{Y}^{(1)}}_{\text{achiral,apolar}} \underbrace{- \Omega_i^{\mathcal{A}} \times \boldsymbol{\rho}_i - \frac{1}{60}\boldsymbol{\epsilon} \cdot \mathbf{V}_i^{(4a)} \cdot \mathbf{Y}^{(3)}}_{\text{chiral,polar}}, \tag{2}$$

have coefficients of polar, apolar, and chiral symmetry. Here $\boldsymbol{\epsilon}$ is the Levi-Civita tensor. The retained modes have physical interpretations: for a single colloid in an unbounded fluid, $\mathbf{V}^{\mathcal{A}}$ $(l\sigma = 1s)$ and $\Omega^{\mathcal{A}}$ $(l\sigma = 2a)$ are the linear and angular velocities in the absence of external forces and torques, $\mathbf{V}^{(2s)}$ is the active contribution to the stresslet, while $\mathbf{V}^{(3a)}$, $\mathbf{V}^{(3t)}$, and $\mathbf{V}^{(4a)}$ are strengths of the chiral torque dipole, polar vector quadrupole, and chiral octupole, respectively. The tensors are parametrized uniaxially, $\mathbf{V}_i^{\mathcal{A}} = v_s \mathbf{p}_i, \Omega_i^{\mathcal{A}} = \omega_s \mathbf{p}_i$, $\mathbf{V}_i^{(2s)} = V_0^{(2s)}[\mathbf{p}_i \mathbf{p}_i - (\mathbf{I}/3)]$ and so on, where v_s and ω_s are speeds of active translation and rotation and $V_0^{(2s)}$ positive (negative) corresponds to a pusher (puller). The relation of these modes to exterior fluid flow and Stokes multipoles is explained in Ref. [9].

The synthetic active colloids in Ref. [1] are polar and achiral (they self-propel but do not spin), while the bacteria in Ref. [2] are polar and chiral (they self-propel and spin). Both these cases are included in the leading contributions. In Ref. [7] a procedure is outlined for estimating the leading coefficients from experimentally measured flows and it is shown that the active flow produced by flagellates and green algae can be modeled by slip. Our model is of sufficient generality, then, to include both synthetic and biological active colloids, and situations where swirling and time-dependent slip may be necessary [16].

Active forces and torques.—Newton's equations of motion for the colloids reduce, when inertia is negligible, to instantaneous balance of forces and torques

$$\mathbf{F}_i^H + \mathbf{F}_i^P + \boldsymbol{\xi}_i^T = 0, \qquad \mathbf{T}_i^H + \mathbf{T}_i^P + \boldsymbol{\xi}_i^R = 0. \tag{3}$$

Here, $\mathbf{F}_i^H = \int \mathbf{f} d\mathrm{S}_i$, $\mathbf{F}^P$ and $\boldsymbol{\xi}^{\mathbf{T}}$ are, respectively, the hydrodynamic, body and Brownian forces, while, $\mathbf{T}_i^H = \int \boldsymbol{\rho}_i \times \mathbf{f} d\mathrm{S}_i$, $\mathbf{T}_i^P$ and $\boldsymbol{\xi}_i^R$ are corresponding torques, $\boldsymbol{\sigma}$ is the Cauchy stress in the fluid, and $\mathbf{f} = \hat{\boldsymbol{\rho}}_i \cdot \boldsymbol{\sigma}$ is the traction. The linearity of the Stokes equation implies that these must be of the form

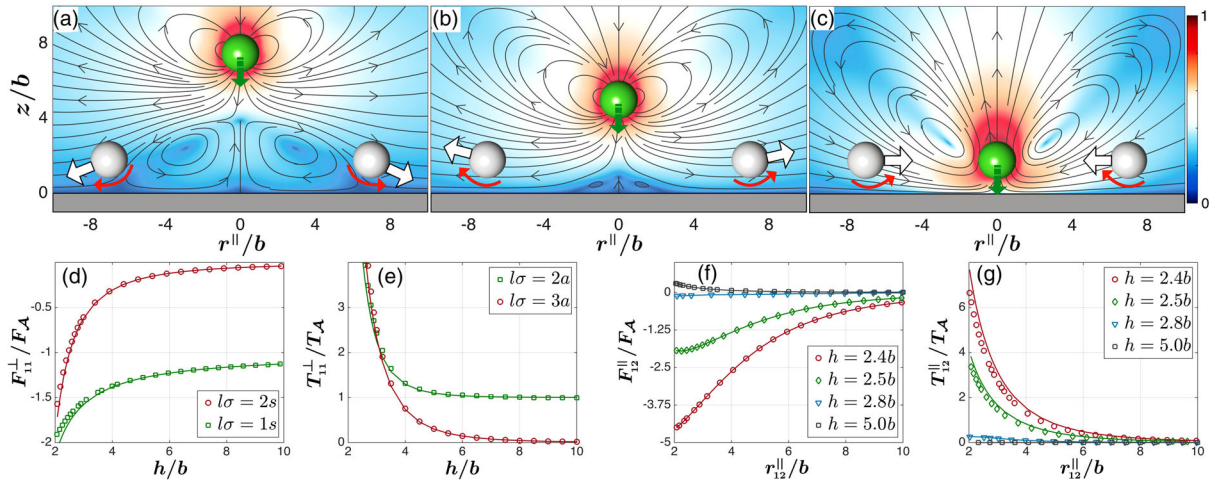

FIG. 2. Distortion of the flow produced by leading polar ($l\sigma = 1s$) and apolar ($l\sigma = 2s$) slip terms in Eq. (2) as an active colloid of radius b, shown in green, approaches a plane wall. Tracer colloids are show in white. The streamlines of fluid flow have been overlaid on a pseudocolor plot of logarithm of the magnitude of the local flow normalized by its maximum. The flow in (c) results when the colloid is brought to rest near the wall. Hydrodynamic forces attract nearby colloids, as shown by thick white arrows, leading to crystallization. Hydrodynamic torques tend to reorient the colloids as shown by curved red arrows. The remaining graphs show quantitative variation of active forces and torques from modes in Eq. (2) scaled by $F_{\mathcal{A}} = 6\pi\eta b v_s$ and $T_{\mathcal{A}} = 8\pi\eta b^2 v_s$ respectively as a function of height h of the colloid from the wall and distance, $\mathbf{r}_{ij} = \mathbf{R}_i - \mathbf{R}_j$, from other colloids. Solid and dotted lines represent analytical and numerical results, respectively (see text). Here, $\parallel$ and $\perp$ indicate directions parallel and perpendicular to the wall at $\mathbf{z} = 0$.

$$\mathbf{F}_i^H = -\boldsymbol{\gamma}_{ij}^{TT}\cdot V_j - \boldsymbol{\gamma}_{ij}^{TR}\cdot\Omega_j - \sum_{l\sigma=1s}^{\infty} \boldsymbol{\gamma}_{ij}^{(T,l\sigma)} \cdot \mathbf{V}_j^{(l\sigma)}, \quad \text{(4a)}$$

$$\mathbf{T}_i^H = -\boldsymbol{\gamma}_{ij}^{RT}\cdot\mathbf{V}_j - \boldsymbol{\gamma}_{ij}^{RR}\cdot\Omega_j - \sum_{l\sigma=1s}^{\infty} \boldsymbol{\gamma}_{ij}^{(R,l\sigma)} \cdot \mathbf{V}_j^{(l\sigma)}, \quad \text{(4b)}$$

where repeated particle indices are summed over. The $\boldsymbol{\gamma}_{ij}^{\alpha\beta}$, with $\alpha, \beta = T, R$, are the usual friction matrices associated with rigid body motion and $\boldsymbol{\gamma}_{ij}^{(\alpha,l\sigma)}$ are friction tensors associated with the irreducible modes of the active slip. They are of rank $l+1$, l, and $l-1$, respectively, for $\sigma = s, a, t$. The forces and torques depend on relative position (through the $\boldsymbol{\gamma}_{ij}^{(\alpha,l\sigma)}$) and on relative orientation (through the $\mathbf{V}_j^{(l\sigma)}$). Their signature under time reversal shows that the active contributions are dissipative.

We calculate the friction tensors using a Galerkin discretization of the boundary integral equation [7] with the Lorentz-Blake Green's function [17] which, by construction, vanishes at the plane wall. The $\boldsymbol{\gamma}_{ij}^{(T,l\sigma)}$ decay as $r_{ij}^{-(l+1)}$ and $r_{ij}^{-(l+2)}$ in directions parallel and perpendicular to the wall. The $\boldsymbol{\gamma}_{ij}^{(R,l\sigma)}$ decay one power of r_{ij} more rapidly. While the force and torque so obtained are sufficient to study colloidal motion, additional insight is obtained from studying the flow, which we compute from its boundary integral representation. Further details are given in Ref. [9].

The modes $l\sigma = 1s$ and $l\sigma = 2a$ contribute most dominantly to forces and torques and they attain their lower bounds far away from the wall, where their magnitudes are $F = 6\pi\eta b v_s$ and $T = 8\pi\eta b^3\omega_s$. The bacteria in Ref. [2] have radius $b \sim 4\ \mu$m, swimming speed $v_s \sim 500\ \mu$m/s, and angular speed $\omega_s \sim 50\ \text{s}^{-1}$ in a fluid of viscosity $\eta = 10^{-3}$ kg/ms. This gives an estimate of $F \sim 40 \times 10^{-12}$ N and $T \sim 10^{-16}$ Nm. For the synthetic colloids in Ref. [1], $b \sim 2\ \mu$m, $v_s \sim 10\ \mu$m/s, which corresponds to $F \sim 10^{-13}$ N. Typical Brownian forces and torques are of order $\mathcal{O}(k_BT/b) \sim 10^{-15}$ N, and $\mathcal{O}(k_BT) \sim 10^{-21}$ N m, respectively. Thus, active forces and torques overwhelm Brownian contributions by factors of 100 or more in these experiments and, henceforth, we neglect their effects. Trajectories are obtained by integrating the kinematic equations $\dot{\mathbf{R}}_i = \mathbf{V}_i$ and $\dot{\mathbf{p}}_i = \Omega_i \times \mathbf{p}_i$, where $\mathbf{V}_i$ and Ω_i satisfy Eq. (3) with Brownian contributions removed. Integration methods and parameter choices are detailed in Ref. [9].

Crystallization kinetics.—The kinetics of crystallization obtained from numerical solutions is shown in movie 1 of the Supplemental Material [9], together with the evolution of the structure factor $S(\mathbf{k})$. The uniform state is destabilized, most notably for any initial density, by attractive active hydrodynamic forces. Steric repulsion between particles balances these to produce crystallites with hexagonal positional order. Rings in the structure factor first appear at wave numbers that correspond to Bragg vectors of the lattice, reminiscent of a spinodal instability, representing the averaged scattering from randomly oriented crystallites. These sharpen into Bragg peaks as crystallites coalesce and orientational order grows. Finally, particles assemble into a single crystallite which continues to rotate, while the structure factor shows a clear sixfold symmetry. In the Supplemental Material, movie 2 [9] we show the formation of a hexagonal unit cell from

the simulation of seven polar and chiral active colloids. The crystallite rotates with an angular velocity parallel to the chiral axis of the colloids.

Universal mechanisms.—To better understand the mechanisms behind active crystallization we show, in Fig. (2), the active flow near a wall and the dominant contributions to the flow-mediated forces and torques. The top three panels show the increasing distortion of the flow produced by the leading polar ($l\sigma = 1s$) and apolar ($l\sigma = 2s$) modes of the slip for $\mathbf{p}_i$ normal to the wall and $V_0^{(2s)} < 0$. The flow develops a monopolar character as the colloid is brought to rest at a height h by the balance of hydrodynamic attraction, Fig. 2(d), and steric repulsion from the wall. The induced monopole on the colloids leads to attractive forces between them below a critical height h from the wall as shown in Fig. 2(f). Nearby colloids entrained in this flow are attracted towards the central colloid as shown in the rightmost panel and in the Supplemental Material, movie 3 [9]. The balance of the hydrodynamic attraction and steric repulsion determines the lattice spacing d. We note that even an apolar colloid is attracted to the wall, Fig. 2(d), and induces hydrodynamic attractive forces. Thus, unlike MIPS [5], polarity is not necessary for crystallization. The induced monopole also tends to reorient the colloids, by generating a torque in the plane of the wall, as shown by curved red arrows in Fig. 2(c) and quantified in Fig. 2(g). Their destabilizing effect can be nullified by external torques $\mathbf{T}^P = T_0(\hat{z} \times \mathbf{p}_i)$ in the plane of the wall due to bottom heaviness. The orientation can also be stabilized by the chiral terms in Eq. (2), which produce torques $\perp$ to the wall, as shown in Fig. 2(e). This chiral torque acting $\perp$ to the wall, when combined with destabilizing torque $\parallel$ to the wall, induces *active* precession of the orientation about the wall normal, thereby stabilizing the orientations. The role of each of the six terms in Eq. (2) in generating positional order, orientational order, and crystal rotation is tabulated in Ref. [9]. Activity *and* body forces pointing away from the wall are necessary for positional order while bottom heaviness *or* chirality is necessary for orientational stability.

Harmonic excitations.—We now study harmonic excitations $\mathbf{u}_i$ of a perfect hexagonal crystal by expanding the positions as $\mathbf{R}_i = \mathbf{R}_i^0 + \mathbf{u}_i$ around the stationary state $\mathbf{R}_i^0 = (X_i^0, Y_i^0, h)$ and ignoring orientational fluctuations. Force balance to leading order gives

$$-\boldsymbol{\gamma}_{ij}^{TT} \cdot \dot{\mathbf{u}}_j + (\boldsymbol{\nabla}_j \boldsymbol{\gamma}_{ij}^{TT} \cdot \mathbf{V}^{\mathcal{A}} - \mathbf{D}_{ij}) \cdot \mathbf{u}_j = 0, \tag{5}$$

where $\mathbf{D}_{ij} = -\boldsymbol{\nabla}_j \boldsymbol{\nabla}_i U|_0$ and U is the sum of all steric potentials. This shows that relaxation is determined by both activity and elasticity, unlike in an equilibrium colloidal crystal where elasticity alone relaxes strains. The normal modes of relaxation can be obtained by Fourier transforming in the plane and in time. The dispersion is found from solutions of

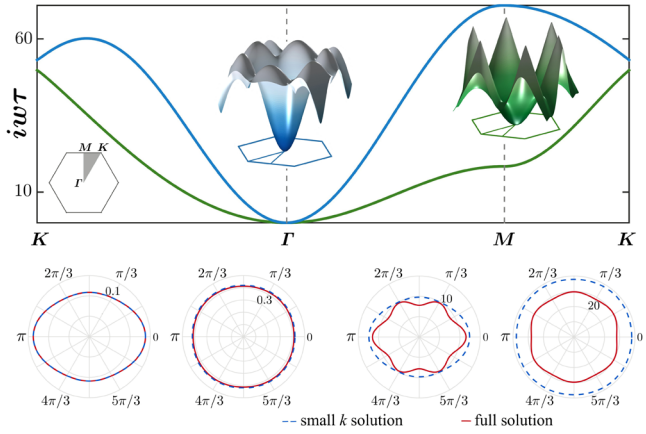

FIG. 3. Branches of the dispersion relation for the two planar normal modes of relaxation of a hexagonal active crystal. The curves in the upper panel show the dispersion along high symmetry directions of the Brillouin zone (first inset). The surfaces in the second and third insets show the dispersion over the entire Brillouin zone. Polar plots in the lower panel have comparisons of the full numerical solution of Eq. (6) with the approximate solution at small k of Eq. (7) for $k = 0.01k_0$ (left panel) and $k = 0.3k_0$ (right panel).

$$\det|-i\omega\boldsymbol{\gamma}_{\mathbf{k}}^{TT} + i\mathbf{k}\boldsymbol{\gamma}_{\mathbf{k}}^{TT} \cdot \mathbf{V}^{\mathcal{A}} - \mathbf{D}_{\mathbf{k}}| = 0. \tag{6}$$

Here, $\mathbf{k} = (k_1, k_2)$ is the wave vector restricted to the first Brillouin zone [9], ω is the frequency, and $\mathbf{D}_{\mathbf{k}}$ is the dynamical matrix. The pair of dispersion relations for motion parallel to the wall are shown in Fig. (3). The dispersion for $k \ll k_0$ is quadratic in wave number

$$\omega_{\pm} = -i\frac{\gamma_{\perp}^T h v_s}{2\gamma_{\parallel}^T} f_{\pm}(\theta) k^2, \tag{7}$$

where $f_{\pm}(\theta)$ are angular factors, $\gamma_{\parallel}^T$ and $\gamma_{\perp}^T$ are one-body frictions parallel and perpendicular to the wall, and $\tan\theta = (k_2/k_1)$. The small-k approximation is compared with the numerical solution in Fig. (3) and it is found to hold for $k \lesssim 0.1k_0$. These can be interpreted as overdamped phonon modes of the active crystal [18]. The presence of the active term $i\mathbf{k}\boldsymbol{\gamma}_{\mathbf{k}}^{TT} \cdot \mathbf{V}^{\mathcal{A}}$ in Eq. (6) makes them differ from phonon modes of a colloidal crystal.

Discussion.—In this work, we have considered only hydrodynamic forces and torques, unlike the case of MIPS [5], where Brownian torques drives reorientations [6]. We have shown that the latter are at least 2 orders of magnitude weaker than the former for experiments in the class of Refs. [1,2]. However, it is conceivable that thermal fluctuations will play a more significant role when the activity is comparatively weak, modifying both the nature of crystallization transition and the stability of the crystalline phase. The spinodal-like instability appears due to the uncompensated long-ranged attractive active forces. These can be compensated by entropic forces to stabilize the disordered phase at finite temperatures. A nucleational route to crystallization, with activity-enhanced rates, is then

possible in the regime where the active forces reduce the nucleation barrier without driving it to zero. In the crystalline phase, thermal fluctuations will excite both phonon and topological modes. Phonon fluctuations will destroy long-range translational order [20], but due to the activity-enhanced stiffness of these modes, large system sizes (compared to equilibrium) will be needed to observe the power-law decay of correlations. Topological defects will be excited at higher temperatures and a defect unbinding transition [21–25], modified by activity, may destroy translational order entirely, producing instead an "active" hexatic phase. These present exciting avenues for future research. We remark that wall-bounded clustering phenomena in algae [26] and charged colloids [27] are mediated by specific forms of the universal hydrodynamic mechanisms presented here.

Finally, we suggest that the flow-induced phase separation found here may provide a paradigm, complementary to MIPS, in which theoretical and experimental studies of momentum-conserving driven [28] and active matter [29–34] may be situated.

We thank M. E. Cates, P. Chaikin, D. Frenkel, D. J. Pine, A. Laskar, and T. V. Ramakrishnan for helpful discussions and IMSc for computing resources on the Nandadevi clusters.

*rsingh@imsc.res.in
†rjoy@imsc.res.in

[1] J. Palacci, S. Sacanna, A. P. Steinberg, D. J. Pine, and P. M. Chaikin, Science **339**, 936 (2013).
[2] A. P. Petroff, X.-L. Wu, and A. Libchaber, Phys. Rev. Lett. **114**, 158102 (2015).
[3] A. Einstein, Ann. Phys. (Berlin) **322**, 549 (1905).
[4] R. Kubo, Rep. Prog. Phys. **29**, 255 (1966).
[5] J. Tailleur and M. E. Cates, Phys. Rev. Lett. **100**, 218103 (2008); M. E. Cates, D. Marenduzzo, I. Pagonabarraga, and J. Tailleur, Proc. Natl. Acad. Sci. U.S.A. **107**, 11715 (2010); M. E. Cates and J. Tailleur, Eur. Phys. Lett. **101**, 20010 (2013); Annu. Rev. Condens. Matter Phys. **6**, 219 (2015).
[6] S. Henkes, Y. Fily, and M. C. Marchetti, Phys. Rev. E **84**, 040301 (2011); Y. Fily and M. C. Marchetti, Phys. Rev. Lett. **108**, 235702 (2012); J. Bialké, T. Speck, and H. Löwen, Phys. Rev. Lett. **108**, 168301 (2012); G. S. Redner, M. F. Hagan, and A. Baskaran, Phys. Rev. Lett. **110**, 055701 (2013).
[7] S. Ghose and R. Adhikari, Phys. Rev. Lett. **112**, 118102 (2014).R. Singh, S. Ghose, and R. Adhikari, J. Stat. Mech. (2015) P06017; R. Singh and R. Adhikari, arXiv:1603.05735.
[8] Slip may have arbitrary radial and tangential components, but surface cannot be a source or sink.
[9] See Supplemental Material at http://link.aps.org/supplemental/10.1103/PhysRevLett.117.228002, which includes Refs. [10–15], for movies of crystallization, detailed calculations, and plots of fluid flow.
[10] F. K. G. Odqvist, Math. Z. **32**, 329 (1930); O. A. Ladyzhenskaia, *The Mathematical Theory of Viscous Incompressible Flow*, Mathematics and its Applications (Gordon and Breach, New York, 1969); C. Pozrikidis, *Boundary Integral and Singularity Methods for Linearized Viscous Flow* (Cambridge University Press, Cambridge, England, 1992); S. Kim and S. J. Karrila, *Microhydrodynamics: Principles and Selected Applications* (Butterworth-Heinemann, London, 1992); P. Mazur and W. van Saarloos, Physica (Amsterdam) **115A**, 21 (1982); S. Hess and W. Köhler, *Formeln zur Tensor-Rechnung* (Palm & Enke, Germany, 1980); A. J. C. Ladd, J. Chem. Phys. **88**, 5051 (1988); P. Brunn, Rheol. Acta **15**, 104 (1976); R. Schmitz, Physica (Amsterdam) **102A**, 161 (1980).
[11] M. Born and K. Huang, *Dynamical Theory of Crystal Lattices* (Clarendon Press, Oxford, 1954).
[12] R. Singh, A. Laskar, and R. Adhikari, PyStokes: Hampi (2014).
[13] M. Skoge, A. Donev, F. H. Stillinger, and S. Torquato, Phys. Rev. E **74**, 041127 (2006).
[14] H. P. Langtangen and L. Wang, Odespy (2012).
[15] J. D. Weeks, D. Chandler, and H. C. Andersen, J. Chem. Phys. **54**, 5237 (1971).
[16] K. Drescher, R. E. Goldstein, N. Michel, M. Polin, and I. Tuval, Phys. Rev. Lett. **105**, 168101 (2010); K. Drescher, J. Dunkel, L. H. Cisneros, S. Ganguly, and R. E. Goldstein, Proc. Natl. Acad. Sci. U.S.A. **108**, 10940 (2011); J. S. Guasto, K. A. Johnson, and J. P. Gollub, Phys. Rev. Lett. **105**, 168102 (2010); R. E. Goldstein, Annu. Rev. Fluid Mech. **47**, 343 (2015).
[17] J. R. Blake, Proc. Cambridge Philos. Soc. **70**, 303 (1971).
[18] Including fluid unsteadiness can produce underdamped phonons, as was pointed out in Ref. [19] for passive colloids.
[19] J. F. Joanny, J. Colloid Interface Sci. **71**, 622 (1979).
[20] R. Peierls, Ann. I. H. Poincaré **5**, 177 (1935); L. D. Landau, Phys. Z. Sowjetunion **11**, 26 (1937).
[21] J. M. Kosterlitz and D. J. Thouless, J. Phys. C **6**, 1181 (1973).
[22] B. I. Halperin and D. R. Nelson, Phys. Rev. Lett. **41**, 121 (1978).
[23] D. R. Nelson and B. I. Halperin, Phys. Rev. B **19**, 2457 (1979).
[24] A. P. Young, Phys. Rev. B **19**, 1855 (1979).
[25] P. M. Chaikin and T. C. Lubensky, *Principles of Condensed Matter Physics* (Cambridge University Press, Cambridge, England, 2000), Vol. 1.
[26] K. Drescher, K. C. Leptos, I. Tuval, T. Ishikawa, T. J. Pedley, and R. E. Goldstein, Phys. Rev. Lett. **102**, 168101 (2009).
[27] T. M. Squires, J. Fluid Mech. **443**, 403 (2001).
[28] K. Yeo, E. Lushi, and P. M. Vlahovska, Phys. Rev. Lett. **114**, 188301 (2015).
[29] M. Trau, D. A. Saville, and I. A. Aksay, Science **272**, 706 (1996).
[30] Y. Solomentsev, M. Böhmer, and J. L. Anderson, Langmuir **13**, 6058 (1997).
[31] R. Matas-Navarro, R. Golestanian, T. B. Liverpool, and S. M. Fielding, Phys. Rev. E **90**, 032304 (2014).
[32] A. Pandey, P. B. Sunil Kumar, and R. Adhikari, Soft Matter, doi:10.1039/C6SM02104B (2016).
[33] W. Wang, W. Duan, S. Ahmed, A. Sen, and T. E. Mallouk, Acc. Chem. Res. **48**, 1938 (2015).
[34] M. S. D. Wykes, J. Palacci, T. Adachi, L. Ristroph, X. Zhong, M. D. Ward, J. Zhang, and M. J. Shelley, Soft Matter **12**, 4584 (2016).